applied optics

Aperture design for a dark-field wafer defect inspection system

Chao Liu,[1,2] Shuang Xu,[1,2,3,*] Yufei Liu,[1,3] and Zainan Xiao[2]

[1]Key Laboratory of Metallurgical Equipment and Control Technology, Ministry of Education, Wuhan University of Science and Technology, Wuhan 430081, China
[2]Hubei Key Laboratory of Mechanical Transmission and Manufacturing Engineering, Wuhan University of Science and Technology, Wuhan 430081, China
[3]Precision Manufacturing Institute, Wuhan University of Science and Technology, Wuhan 430081, China
*Corresponding author: shuangxu@wust.edu.cn

Received 13 September 2021; revised 7 November 2021; accepted 8 November 2021; posted 9 November 2021 (Doc. ID 443118); published 3 December 2021

The dark-field defect inspection system occupies 70% of the market in the field of unpatterned wafer inspection. But the detection limit is still restrained by the haze signals. Signal-to-noise ratio (SNR) enhancement could effectively decrease the detection limit by decreasing the influence of the haze signals on the defect signals. The existing method of optimizing the inspection conditions, including beam path and collection channel, can enhance the SNR, but the effect is restrained by the system structure. The empirically designed aperture has been attempted to be used by blocking the scattering signals in a certain azimuth angle range. However, the performance is restrained, as a signal with a large SNR exists in the blocked scattering signals. In this paper, we propose a novel (we believe) aperture design method in the light of scattering field analysis to reduce the influence of the haze signals caused by the wafer surface roughness on the particle signals. On the basis of the bidirectional reflectance distribution function, apertures are designed according to the ratio field of the particle signal to haze and verified by the scattering model developed based on the tools of the National Institute of Standards and Technology. Additionally, incident conditions are optimized according to their influence on the SNR. It is noteworthy that the aperture designed under specific conditions cannot be used for all particles. Three aperture combination schemes are proposed in this paper, which can ensure the scattering characteristics such as intensity and sensitivity to meet the system requirements while improving the contrast. Simulation results verify that the detection limit decreases from 48 to 22 nm by introducing a well-designed aperture, with the case of *p*-polarized incident light when the threshold is 3 and the incident angle is 72°. Multiaperture schemes have better performance over others, especially the one-to-one scheme.

https://doi.org/10.1364/AO.443118

1. INTRODUCTION

When the semiconductor node decreases, high-precision inspection instruments are required for defect detection in manufacturing. Unpatterned wafer surface defect is a hot issue in semiconductor inspection. Killer defects such as particles, scratches, pits, and air pockets are formed in the process of the wafer production, which will reduce the yield of chip manufacturing [1]. These defects need to be detected during high-throughput and high-precision inspection [2].

Optical inspection and E-beam inspection are the two widely used techniques. Due to the picometer scale wavelength source adopted, E-beam systems have a wider range of dynamic resolution and higher precision than optical systems [3,4]. PROVision 2 E eBeam Inspection, developed by Applied Materials, can reach the detect limit of 1 nm [5]. But the efficiency of the E-beam inspection system is not as expected. For the defects of 16 nm node, an E-beam system needs about 80–160 h to inspect a 101.6 mm wafer [6]. An optical system only spends about 4–8 h for the same issue and can realize the high-speed inspection of nanometer scale defects [7]. In the optical inspection equipment market, products by KLA-Tencor Corporation account for the majority. Among them, the Surfscan series, based on light scattering, is widely used for unpatterned wafer defect inspection [8]. At present, the detection limit of the latest product SP7 is 12.5 nm, which cannot reach the critical dimension of less than 10 nm [7,9]. The detection limit of optical inspection systems can be reduced through SNR enhancement techniques.

Dark-field inspection systems detect particles by collecting the scattered signals from the wafer surface [10–12]. Haze signal, formed due to the roughness of the wafer surface, is also inevitably collected, which is the main factor that affects the precision of the inspection systems. As shown in Fig. 1, the scattered

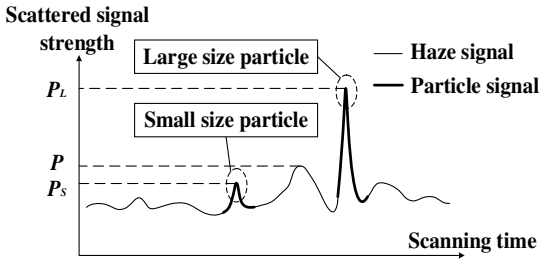

Fig. 1. Distribution of the scattered signals on the wafer surface.

signal of a small particle gets lost in the haze signal, since the two kinds of signals are mixed, thus the detection limit cannot be further reduced. Optimizing the inspection conditions, including beam path and collection channel, can enhance the SNR, but the effect is restrained by the system structure [13]. Ideal extreme incident angles cannot be realized and the detector cannot collect the ultimate scattered signals. An aperture is supposed to be an effective and implementable optical component to apply to the dark-field scattering equipment to reduce the influence of the haze signals [14]. Some scattered signals are blocked by adding a tentative aperture in the beam path, but the pattern and the strategy of the introduced aperture and the effect remain to be studied.

This paper proposes a novel aperture design method based on the signal ratio field of the particle to the haze [15–17]. The scattering fields are calculated on the basis of the bidirectional reflectance distribution function (BRDF) [18–20]. The ratio field of the scattering fields is divided into two regions with the threshold as boundary, and the aperture pattern is obtained by projecting regions to the two-dimensional plane. The aperture is designed and analyzed with the scattering fields simulated based on the tools by National Institute of Standards and Technology (NIST) [21]. The influence of incident parameters on the aperture performance is analyzed to optimize the measurement conditions. In order to make it available for the actual inspection process, three aperture combination design schemes are proposed to stabilize scattering characteristics such as intensity and sensitivity while enhancing the SNR.

2. THEORY OF APERTURE DESIGN

In this paper, an aperture design method based on the Mie scattering theory [22–24] is proposed. The intensity distribution of scattered signal is related to the shape, size, and material of the defects, as well as environmental factors such as wafer material and wavelength. Due to the fact that particles are the most common defects on the wafer surface and there is a complete scattering theory and calculation method for particles, this paper verifies the feasibility of the aperture design method using particles as the object.

A. Scattering Field Model

The scattering field of the particle and haze is calculated by BRDF, which is related to factors such as wavelength, the polarization state of the light, and the refractive indices of the particle and the substrate [13–15].

Considering the case with one single particle on the wafer surface, the geometric parameters of the scattering field are defined as in Fig. 2. The angle between the incident light and the surface normal is the incident angle θ_i, with the incident plane defined as this plane. The scattering plane is formed with the scattered light and the surface normal, and the angle between these two is the scattering angle θ_s. The azimuth angle φ_s is defined as the angle between the incident plane and the scattering plane. The s polarization state of the incident light is perpendicular to the incident plane, while the p polarization state is in the incident plane and perpendicular to the incident direction.

The scattered intensity of the particles located on the smooth wafer surface in the unit azimuth can be calculated by

$$\Delta P_{\text{particle}} = \Delta\Omega P_i \cos\theta_s \,\text{BRDF}_{\text{particle}}, \tag{1}$$

$$\text{BRDF}_{particle} = \frac{16\pi^4}{\lambda^4}\left(\frac{n_p^2-1}{n_p^2+2}\right)^2 \frac{R^6}{\cos\theta_s\cos\theta_i}\frac{NF}{A}|Q_{ij}\cdot\hat{e}|^2, \tag{2}$$

where $\Delta P_{\text{particle}}$ is the unit scattered power of the particles, ΔP_i is the unit incident light power, $\Delta\Omega$ is the unit azimuth, λ is the wavelength of incident light, R is the particle radius, n_p is the particle refractive index, N is the number of particles in spot area A, F is the structure factor, and $\hat{e}$ is the unit vector parallel to the incident field. Q_{ij} is the polarization factor as (i is the polarization of incident light, and j is the polarization of scattered light),

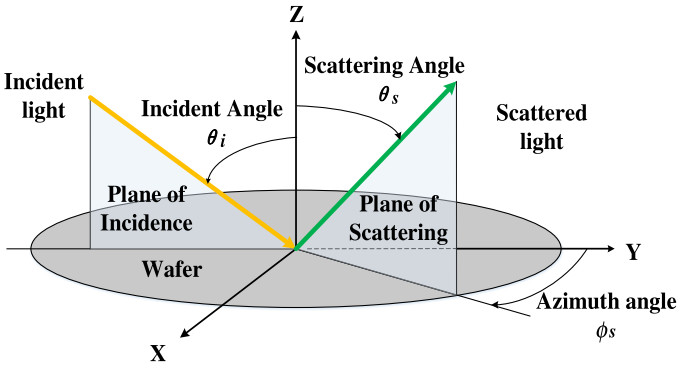

Fig. 2. Schematic diagram of wafer surface scattering field.

$$Q_{ij}=\left\{\begin{array}{c} Q_{ss}=[1+\beta r_s(\theta_s)][1+\alpha r_s(\theta_s)]\cos\varphi_s \\ Q_{sp}=-[1-\beta r_p(\theta_s)][1+\alpha r_s(\theta_i)]\cos\theta_s\sin\varphi_s \\ Q_{pp}=[1+\beta r_p(\theta_s)][1+\alpha r_p(\theta_i)]\sin\theta_i\sin\varphi_s \\ -[1-\beta r_p(\theta_s)][1-\alpha r_p(\theta_i)]\cos\theta_s\cos\theta_i\cos\varphi_s \\ Q_{ps}=-[1+\beta r_s(\theta_s)][1-\alpha r_p(\theta_i)]\cos\theta_i\sin\varphi_s \end{array}\right\}, \tag{3}$$

where $\beta=\exp(2ikd\cos\theta_s)$, $\alpha=\exp(2ikd\cos\theta_i)$, $k=2\pi/\lambda$, d is the distance between the particle center and the wafer surface. r_p and r_s are the Fresnel reflection coefficients, which are represented as

$$r_p(\theta)=\frac{n_{12}^2\cos\theta-(n_{12}^2-\sin^2\theta)^{1/2}}{n_{12}^2\cos\theta+(n_{12}^2-\sin^2\theta)^{1/2}}, \tag{4}$$

$$r_s(\theta)=\frac{\cos\theta-(n_{12}^2-\sin^2\theta)^{1/2}}{\cos\theta+(n_{12}^2-\sin^2\theta)^{1/2}}, \tag{5}$$

where n_{12} is the relative refractive index among the media.

The scattered intensity of the haze signal, caused by microroughness on the wafer surface in the unit azimuth can be calculated by

$$\Delta P_{\text{haze}}=\Delta\Omega P_i\cos\theta_s\,\text{BRDF}_{\text{haze}}, \tag{6}$$

$$\text{BRDF}_{\text{haze}}=\frac{16\pi^2(n^2-1)^2}{\lambda^4}\cos\theta_s\cos\theta_i D(fx,fy)\left|q_{ij}\hat{e}\right|^2, \tag{7}$$

where ΔP_{haze} is the unit scattered light power of the haze, n is the refractive index of the wafer surface, $D(f_x,\ f_y)$ is the surface power spectrum function, and q_{ij} is the polarization factor. The surface power spectrum function $D(f_x,\ f_y)$ [12] based on isotropic uniform distribution is shown as

$$D(fx,fy)=\text{a}/[1+(\text{b}f)^2]^{c/2}, \tag{8}$$

$$f=\sqrt{f_x^2+f_y^2}, \tag{9}$$

$$f_x=\frac{\sin\theta s\cos\phi s-\sin\theta i}{\lambda}, \tag{10}$$

$$f_y=\frac{\sin\theta s\sin\phi s}{\lambda}, \tag{11}$$

where a, b, and c are parameters of the surface power spectrum function. The polarization factor q_{ij} is shown as

$$q_{ij}=\left\{\begin{array}{c} q_{ss}=\frac{\cos\varphi_s}{(\cos\theta_i+\sqrt{n^2-\sin^2\theta_i})(\cos\theta_s+\sqrt{n^2-\sin^2\theta_s})} \\ q_{sp}=\frac{-\sin\varphi_s\sqrt{n^2-\sin^2\theta_s}}{(\cos\theta_i+\sqrt{n^2-\sin^2\theta_i})(n^2\cos\theta_s+\sqrt{n^2-\sin^2\theta_s})} \\ q_{pp}=\frac{\sin\theta_i\sin\theta_s-\cos\varphi_s\sqrt{n^2-\sin^2\theta_i}\sqrt{n^2-\sin^2\theta_s}}{(n^2\cos\theta_i+\sqrt{n^2-\sin^2\theta_i})(\cos\theta_s+\sqrt{n^2-\sin^2\theta_s})} \\ q_{ps}=\frac{-\sin\varphi_s\sqrt{n^2-\sin^2\theta_i}}{(n^2\cos\theta_i+\sqrt{n^2-\sin^2\theta_i})(n^2\cos\theta_s+\sqrt{n^2-\sin^2\theta_s})} \end{array}\right\}. \tag{12}$$

The signal contrast S is established as

$$S=\frac{\Delta P_s^{\text{particle}}}{\Delta P_s^{\text{haze}}}=\frac{\text{BRDF}_{\text{particle}}}{\text{BRDF}_{\text{haze}}}. \tag{13}$$

The intensity distribution of the scattering field is different when the incident conditions are different. Functions of the signal contrast S with different polarization states of incident light can be obtained as

$$S_s=C_0\frac{|Q_{ss}|^2+|Q_{sp}|^2}{\left(|q_{ss}|^2+|q_{sp}|^2\right)D(f_x,\ f_y)}, \tag{14}$$

$$S_p=C_0\frac{|Q_{pp}|^2+|Q_{ps}|^2}{\left(|q_{pp}|^2+|q_{ps}|^2\right)D(f_x,\ f_y)}, \tag{15}$$

where C_0 is represented as

$$C_0=\frac{(n_p^2-1)^2\pi^2R^6NF}{(n_p^2+2)^2(n^2-1)^2A\cos^2\theta_s\cos^2\theta_i}. \tag{16}$$

C_0 is constant when the detecting conditions such as substrate material, particle radius, and spot size are determined. Signal contrast S at each position is only related to the scattering angle θ_s and the azimuth angle ϕ_s.

B. Aperture Design Process

Apertures under specific conditions are designed based on the distribution of the signal contrast S. The design process is divided into four steps, as shown in Fig. 3. The first step is to calculate the scattering field. Second, the aperture is designed based on the intensity distribution of the scattering field. Third, the designed aperture is used for processing the simulated scattering field, and the conditions are optimized by analyzing the feature before and after the aperture is placed. Finally, three aperture schemes with applicability are proposed.

A diagram of the light-scattering field is shown in Fig. 4. According to the signal contrast S, the scattering field is divided into two types, the hollow part with $S \geq$ threshold and the nonhollow part with $S <$ threshold of the aperture.

As shown in Fig. 5, two types of areas of the light-scattering field are projected to the two-dimensional plane. The actual size of the aperture is determined by its actual position in the beam path.

The basic principle of the aperture-induced dark-field defect inspection system is shown in Fig. 6. The photomultiplier tube (PMT) collects the scattered light, while the aperture blocks part of the scattered light. In the system, there are two modes of incidence, normal and oblique, which do not work simultaneously.

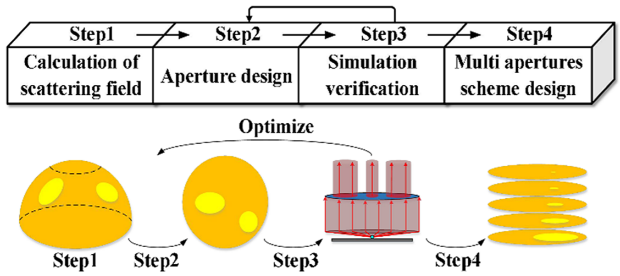

Fig. 3. Aperture design process.

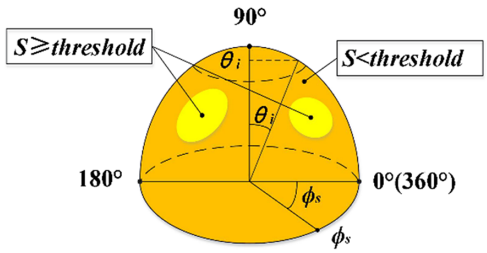

Fig. 4. Region division: the light scattering field is divided into two types, with the threshold as boundary. The area with $S \geq$ threshold is the hollow area, where the scattered light is collected. The area with $S <$ threshold is the nonhollow area, where the scattered light is blocked.

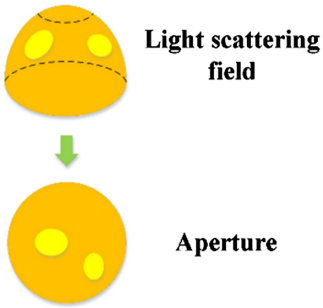

Fig. 5. Aperture design: the pattern of the aperture is designed based on the area division of the scattering field.

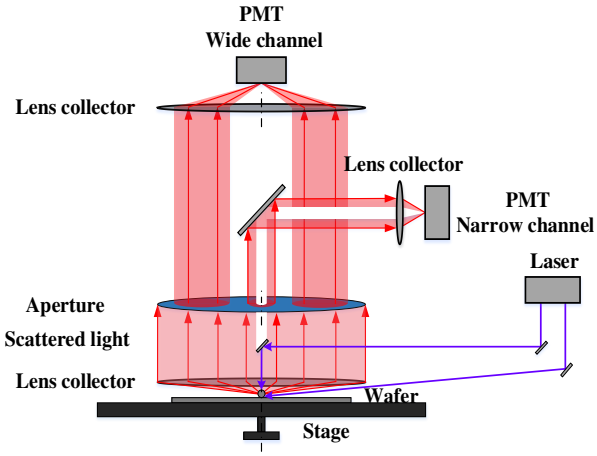

Fig. 6. Schematic diagram of the aperture basic principle.

Different scattering characteristics are obtained by using different incident modes to distinguish defects. The baffles are placed in the optical path to block the reflected light.

3. EXPERIMENTAL RESULTS AND ANALYSIS

The particle scattering model of particles and micro-rough wafer surface is established by tools from NIST. The scattering analysis and the aperture effects are simulated, as is the condition optimization.

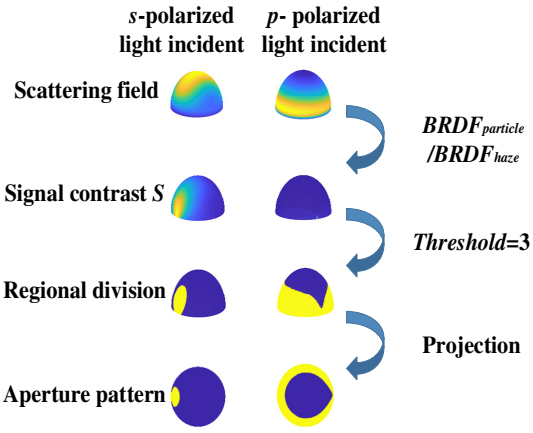

Fig. 7. Whole process of aperture design.

Table 1. Total Signal Contrast S before and after Aperture Is Placed

Simulation Verification	Without Aperture	With Aperture
Signal contrast S	0.5541	6.3391

A. Feasibility Analysis of Aperture

The design parameters of the single aperture are as follows. The incident light is set as p-polarized and s-polarized separately, with the wavelength $\lambda = 488$ nm and the incident angle $\theta_i = 72°$. The silicon wafer surface refractive index $n_2 = 4.3707$ [15]. The threshold of the signal contrast S is set as 3. The particle radius is set as $R = 50$ nm. A polystyrene sphere is currently used as the reference particle in the semiconductor industry, which is also used in the simulation validation of the proposed method, with the refractive index $n_1 = 1.59$.

The aperture design process on the basis of the above parameters is shown in Fig. 7. Among them, the yellow area is the hollow part, and the purple area is the nonhollow part.

The total signal contrast of the scattering field with or without aperture is shown in Table 1, and the signal contrast S is greatly increased when the aperture is placed.

B. Optimization of Incident Conditions

In order to further improve the inspection precision, incident conditions are optimized after the aperture is introduced by analyzing the characteristics of the scattering fields.

The relationship between particle radius R, incident angle θ_i and the total signal contrast S with or without aperture are shown in Fig. 8. The threshold of the signal contrast is set as 3. The detection limit is obtained under the constraints of the light intensity and the signal contrast S. The intensity, which determines whether the detected signal exceeds the threshold of the PMT, should be no less than 10^{-7} as the minimum intensity threshold of the PMT. The detection limit becomes smaller after the aperture is placed. Whether or not the aperture is placed, the detection limit under p-polarized incident light is smaller than that of s-polarized incident light. Setting a larger incident angle can result in getting a larger signal contrast S.

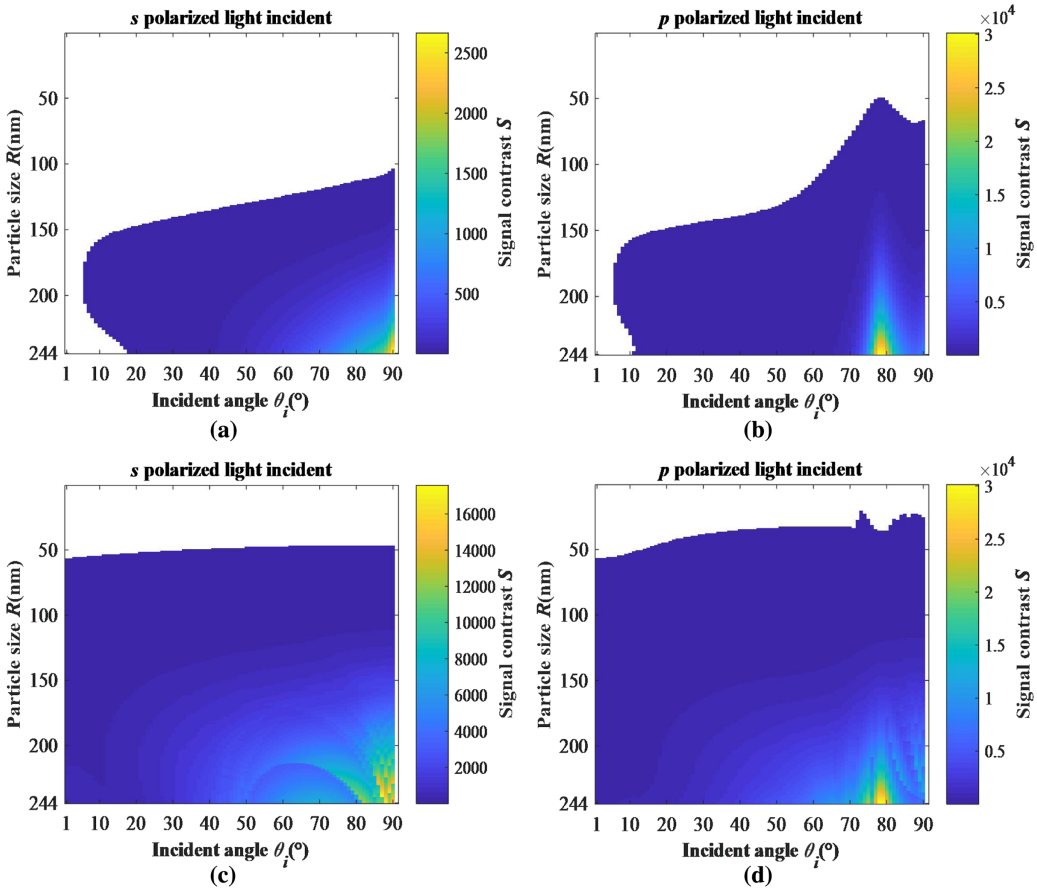

Fig. 8. Total signal contrast of different particle sizes under different incident angles as (a) s-polarized incident light without aperture; (b) p-polarized incident light without aperture; (c) s-polarized incident light with aperture placed; and (d) p-polarized incident light with aperture placed.

Table 2. Optimum Incident Condition

Optimum Condition	Incident Angle	Detection Limit	State of Polarization
Without aperture	s: 90° p: 77°–78°	s: 110 nm p: 48 nm	p
With aperture	s: 61°–90° p: 72°	s: 48 nm p: 22 nm	p

Optimum incident conditions with or without aperture are shown in Table 2, including the incident angle, the polarization state, and the detection limit.

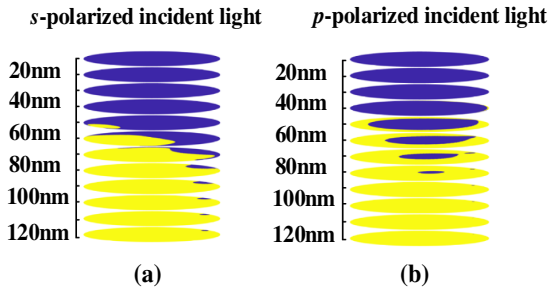

Fig. 9. Change of aperture pattern with R under (a) s-polarized incident light and (b) p-polarized incident light.

C. Aperture Combination Design

In the dark-field defect inspection system, the wafer surface is scanned spirally to receive continuous scattered signal distribution. Meanwhile, different measurement configurations are used to obtain different scattered signal distributions, so as to identify and classify defects. The aperture designed based on specific conditions is not necessarily suitable for the particles of other sizes under other conditions. The wafer scanning process is continuous and repeated, and frequent replacement of the aperture will decrease the inspection efficiency. Therefore, it is necessary to design a reasonable aperture combination scheme for the whole inspection process.

As shown in Fig. 9, aperture patterns corresponding to particles of different sizes are considered in order to design the aperture scheme. The nonhollow area gets smaller as the particle size becomes larger. Three aperture combination schemes are proposed, whose feasibility and performance are verified by simulation.

Three different aperture combination schemes are shown in Fig. 10. The single-aperture scheme is shown in Fig. 10(a), and the aperture is designed by the particle size as the detection limit

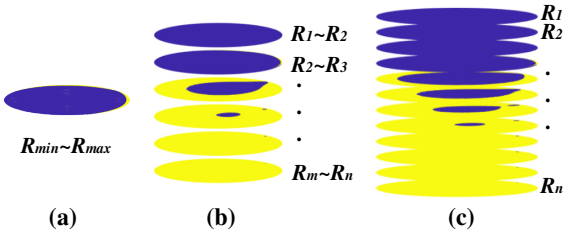

Fig. 10. Different aperture combination schemes as (a) single aperture; (b) multiapertures (one-to-many); and (c) multiapertures (one-to-one).

without aperture. Figure 10(b) shows the "one-to-many" multiaperture scheme, as particles larger than R_{max} can be detected without aperture. The first aperture is designed by R_{max} for the first-round inspection. The second aperture is designed for the second-round inspection, when smaller particles cannot be detected by the first aperture. The step is continued until the last aperture is designed by the detection limit R_{min}. Figure 10(c) shows the other "one-to-one" multiaperture scheme. Starting with R_{max}, each aperture is designed by each particle size.

Apertures should not only improve the signal contrast S, but also ensure the stability of other scattering characteristics, including the intensity and sensitivity of the scattered signals. The intensity of the scattered light is the quantitative standard of defects, which should be larger than the threshold of the PMT to guarantee that the signal can be captured. The sensitivity is an important parameter for distinguishing different sizes and types of defects, as large sensitivity makes the distinguishing easier.

The change of scattering characteristics with and without aperture under Scheme 1 is shown in Fig. 11. After the aperture is placed, the results show that the intensity and sensitivity of scattered light decrease about 3 orders of magnitude, and the signal contrast S increases above the threshold.

The change of scattering characteristics before and after the aperture is placed under Scheme 2 is shown in Fig. 12. The results show that the intensity of scattered light decreases slightly after the aperture is placed, and the signal contrast S increases above the threshold. But the sensitivity has a mutation at the replacement of the aperture.

Figure 13 shows the change of scattering characteristics by the aperture in Scheme 3. After the aperture is placed, the intensity of the scattered light decreases slightly, and the signal contrast S increases above the threshold, and the sensitivity has a mutation. Comparing the three aperture combination schemes, it is obvious that the comprehensive performance of the multiaperture scheme is stabler, especially the one-to-one scheme.

4. CONCLUSION AND FUTURE WORK

In this work, a novel aperture design method for dark-field wafer defect inspection system is proposed. The aperture designed in this paper can be mainly used in a dark-field scattering system, such as the SP series inspection equipment manufactured by KLA, to improve the yield of wafers. Placing the aperture is a simpler and less costly method to reduce detection limit. Compared with the original inspection system under parameters described in this paper, the minimum detection limit decreases from 48 to 22 nm by introducing the designed aperture. Theoretically, this aperture can reduce the detection limit to a certain extent, and the detection limit of SP7 can also be further reduced by placing the aperture, which will be verified by simulation after we got the specific parameters of SP7. Three aperture schemes are proposed and compared. Different aperture schemes can be selected in the light of specific requirements.

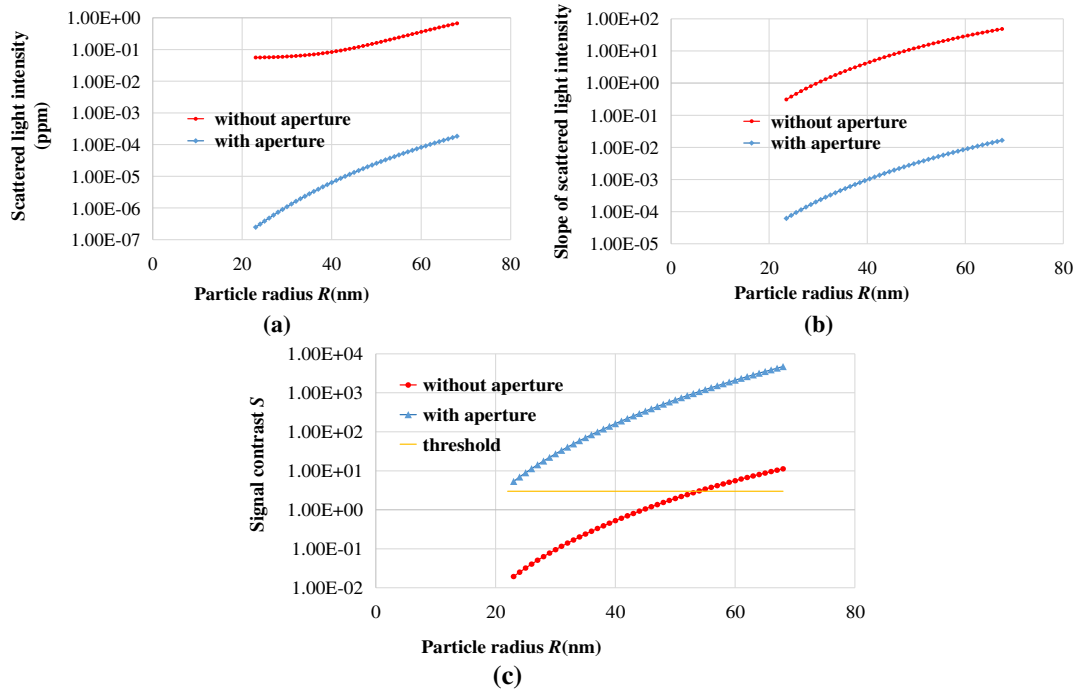

Fig. 11. Single aperture: comparison of scattering characteristics before and after aperture is placed, including (a) scatterred light intensity; (b) slope of scattered light intensity; and (c) signal contrast S.

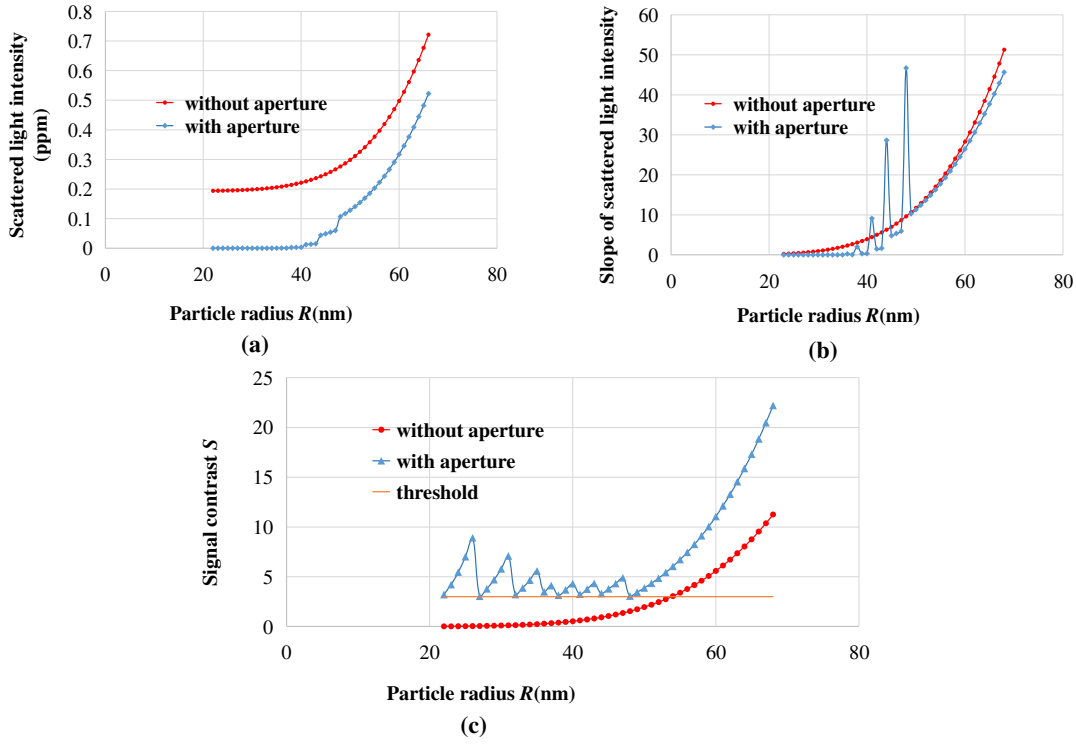

Fig. 12. Multiapertures (one-to-many): comparison of scattering characteristics before and after aperture is placed, including (a) scatterred light intensity; (b) slope of scattered light intensity; and (c) signal contrast S.

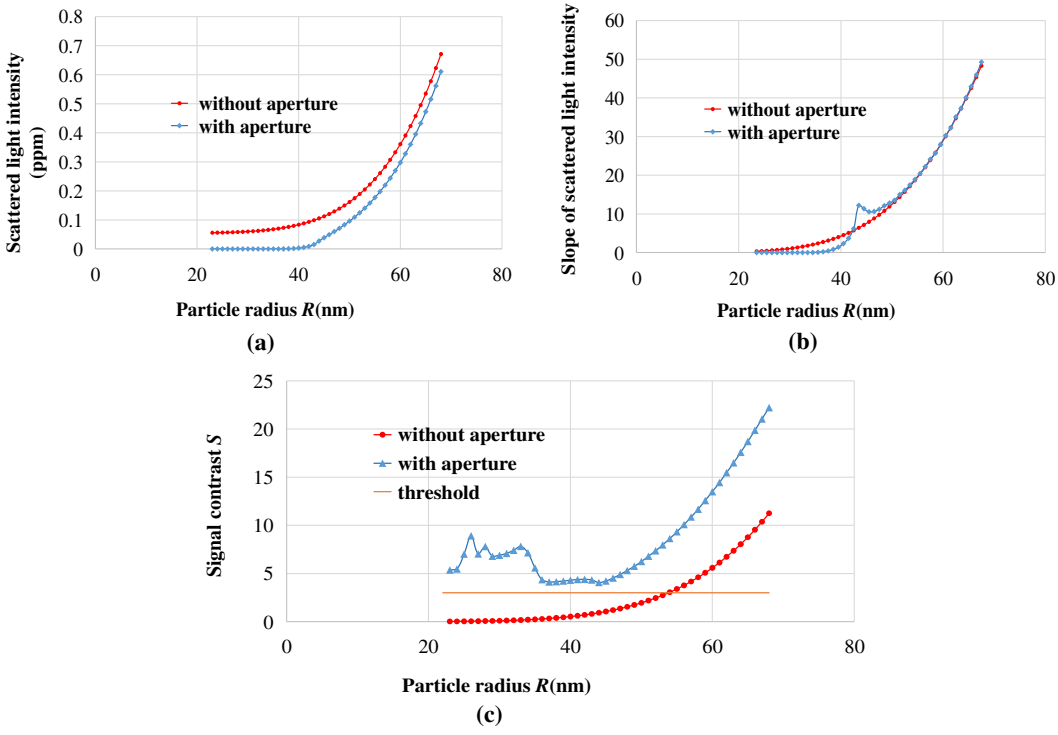

Fig. 13. Multiapertures (one-to-one): comparison of scattering characteristics before and after aperture is placed, including (a) scatterred light intensity; (b) slope of scattered light intensity; and (c) signal contrast S.

Apertures can also be optimized according to the changes of the scattered features such as intensity, sensitivity, and the signal contrast after aperture placed.

In the actual wafer fabrication process, there are many other types of defects besides particles. Different types of defects have different scattering field distribution characteristics. For defects

with regular shapes, including particles, pits, etc., scattering theory can be established and simulation experiments can be performed so that the corresponding aperture can be designed. For irregular defects, the establishment of the theoretical calculation method is a difficult problem. In addition to the defect shape, the material of the defect also affects the scattering characteristics. Various materials used in the process may form defects on the wafer surface. Defects of different materials can cause changes in scattering intensity due to their own refractive indices.

The effect of different types and materials of defects on the scattering characteristics is an important and challenging problem. At present, we have completed simulation experiments on pits and attempted theoretical calculations and have performed some experiments on the properties of silica and silicon materials. In future work, we will refine the study of defect types and materials.

Funding. National Natural Science Foundation of China (12102311, 51905393); Wuhan Zhaoyang Youth Science and Technology Project (202004); Hubei provincial Chenguang Youth Science and Technology Project (2019B08); China Scholarship Council (201808420326).

Acknowledgment. The authors would like to thank the National Institute of Standards and Technology (NIST) for the open-source toolkit.

Disclosures. The authors declare no conflicts of interest.

Data Availability. Data underlying the results presented in this paper are not publicly available at this time but may be obtained from the authors upon reasonable request.

REFERENCES

1. A. Chen, V. Huang, S. Chen, C. J. Tsai, K. Wu, H. Zhang, K. Sun, J. Saito, H. Chen, D. Hu, M. Li, W. Shen, and U. Mahajan, "Advanced inspection methodologies for detection and classification of killer substrate defects," Proc. SPIE **7140**, 1–10 (2008).
2. L. Li, D. Liu, P. Cao, S. Xie, Y. Li, Y. Chen, and Y. Yang, "Automated discrimination between digs and dust particles on optical surfaces with dark-field scattering microscopy," Appl. Opt. **53**, 5131–5140 (2014).
3. J. Z.-C. Lin and S.-T. Juang, "Auto defect screening using adaptive machine learning in semiconductor device manufacturing flow," U.S. patent US20190384236A1 (30 July 2019).
4. O. D. Patterson, J. Lee, D. M. Salvador, S.-C. Lei, and X. Tang, "Detection of sub-design rule physical defects using E-beam inspection," IEEE Trans. Semicond. Manuf. **26**, 476–481 (2013).
5. https://www.appliedmaterials.com/products/provision-ebeam-inspection/.
6. M. Malloy, B. Thiel, B. D. Bunday, S. Wurm, M. Mukhtar, K. Quoi, T. Kemen, D. Zeidler, A. L. Eberl, T. Garbowski, G. Delleman, and J. H. Peters, "Massively parallel e-beam inspection: enabling next-generation patterned defect inspection for wafer and mask manufacturing," Proc. SPIE **9423**, 942319 (2016).
7. A. Oberai and J.-S. Yuan, "Smart E-beam for defect identification & analysis in the nanoscale technology nodes: technical perspectives," Electronics **6**, 87 (2017).
8. A. Romanovsky, I. Maleev, D. Kavaldjiev, Y. Yuditsky, D. Woll, S. Biellak, M. Vaez-Iravani, and G. H. Zhao, "Wafer inspection," U.S. patent US20150369753A1 (24 December 2015).
9. https://www.kla-tencor.com/products/substrate-manufacturing#defect-inspection/.
10. Y. Yang, S. Wang, X. Chen, L. Li, P. Cao, L. Yan, Z. Cheng, and D. Liu, "Sparse microdefect evaluation system for large fine optical surfaces based on dark-field microscopic scattering imaging," Proc. SPIE **8838**, 883806 (2013).
11. G. Lorenzi, K. H. Nguyen, C. Sanna, R. Orizio, and G. Borionetti, "COPs/particles discrimination using an automated surface inspection tool," Proc. SPIE **5041**, 39–49 (2003).
12. G. Videen, J. Y. Hsu, W. S. Bickel, and W. L. Wolfe, "Polarized light scattered from rough surfaces," J. Opt. Soc. Am. A **9**, 1111–1118 (1992).
13. M. S. Kim, H. S. Choi, S. H. Lee, and C. Kim, "A high-speed particle-detection in a large area using line-laser light scattering," Curr. Appl Phys. **15**, 930–937 (2015).
14. Y. Yang, Y. Jeong, M. Numata, M. Park, M. Seo, S. Lee, C. Jun, K. Lee, and I. Cho, "A study of the defect detection technology using the optic simulation for the semiconductor device," Proc. SPIE **8880**, 88801S (2013).
15. L. Gong, Z. S. Wu, Z. J. Li, and G. Zhang, "An improved analysis of the scattering properties of half-space problem with multiple defect particles for an optical surface," J. Quant. Spectrosc. Radiat. Transfer **162**, 184–189 (2015).
16. R. Schmehl, B. M. Nebeker, and E. D. Hirleman, "Discrete-dipole approximation for scattering by features on surfaces by means of a two-dimensional fast Fourier transform technique," J. Opt. Soc. Am. A **14**, 3026–3036 (1997).
17. T. A. Germer, "Angular dependence and polarization of out-of-plane optical scattering from particulate contamination, subsurface defects, and surface microroughness," Appl. Opt. **36**, 8798–8805 (1997).
18. J. C. Stover, *Optical Scattering: Measurement and Analysis* (SPIE, 1995).
19. T. A. Germer, "Polarized light scattering by microroughness and small defects in dielectric layers," J. Opt. Soc. Am. A **18**, 1279–1288 (2001).
20. T. Galpin, R. T. Chartier, N. Levergood, and M. E. Greenslade, "Refractive index retrievals for polystyrene latex spheres in the spectral range 220–420 nm," Aerosol Sci. Technol. **51**, 1158–1167 (2017).
21. T. A. Germer, *Modeled Integrated Scattering Tool (MIST)* (National Institute of Standards and Technology, 2017).
22. W. C. Mundy, J. A. Roux, and A. M. Smith, "Mie scattering by spheres in an absorbing medium," J. Opt. Soc. Am. **64**, 1593–1597 (1974).
23. W. Huebner and Y. Pavlyukh, "Nonlinear Mie scattering from spherical particles," Phys. Rev. B **70**, 245434 (2005).
24. M. Majic and E. C. Le Ru, "Numerically stable formulation of Mie theory for an emitter close to a sphere," Appl. Opt. **59**, 1293–1300 (2020).